

# An absorption profile centred at 78 megahertz in the sky-averaged spectrum

Judd D. Bowman<sup>1</sup>, Alan E. E. Rogers<sup>2</sup>, Raul A. Monsalve<sup>1,3,4</sup>, Thomas J. Mozdzen<sup>1</sup> & Nivedita Mahesh<sup>1</sup>

After stars formed in the early Universe, their ultraviolet light is expected, eventually, to have penetrated the primordial hydrogen gas and altered the excitation state of its 21-centimetre hyperfine line. This alteration would cause the gas to absorb photons from the cosmic microwave background, producing a spectral distortion that should be observable today at radio frequencies of less than 200 megahertz<sup>1</sup>. Here we report the detection of a flattened absorption profile in the sky-averaged radio spectrum, which is centred at a frequency of 78 megahertz and has a best-fitting full-width at half-maximum of 19 megahertz and an amplitude of 0.5 kelvin. The profile is largely consistent with expectations for the 21-centimetre signal induced by early stars; however, the best-fitting amplitude of the profile is more than a factor of two greater than the largest predictions<sup>2</sup>. This discrepancy suggests that either the primordial gas was much colder than expected or the background radiation temperature was hotter than expected. Astrophysical phenomena (such as radiation from stars and stellar remnants) are unlikely to account for this discrepancy; of the proposed extensions to the standard model of cosmology and particle physics, only cooling of the gas as a result of interactions between dark matter and baryons seems to explain the observed amplitude<sup>3</sup>. The low-frequency edge of the observed profile indicates that stars existed and had produced a background of Lyman- $\alpha$  photons by 180 million years after the Big Bang. The high-frequency edge indicates that the gas was heated to above the radiation temperature less than 100 million years later.

Observations with the Experiment to Detect the Global Epoch of Reionization Signature (EDGES) low-band instruments, which began in August 2015, were used to detect the absorption profile. Each of the two low-band instruments consists of a radio receiver and a zenith-pointing, single-polarization dipole antenna. Spectra of the brightness temperature of the radio-frequency sky noise, spatially averaged over the large beams of the instruments, were recorded between 50 MHz and 100 MHz. Raw spectra were calibrated, filtered and integrated over hundreds of hours. Automated measurements of the reflection coefficients of the antennas were performed in the field. Other measurements were performed in the laboratory, including of the noise waves and reflection coefficients of the low-noise amplifiers and additional calibration constants. Details of the instruments, calibration, verification and model fitting are described in Methods.

In Fig. 1 we summarize the detection. It shows the spectrum observed by one of the instruments and the results of model fits. Galactic synchrotron emission dominates the observed sky noise, yielding a power-law spectral profile that decreases from about 5,000 K at 50 MHz to about 1,000 K at 100 MHz for the high Galactic latitudes shown. Fitting and removing the Galactic emission and ionospheric contributions from the spectrum using a five-term, physically motivated foreground model (equation (1) in Methods) results in a residual with a root-mean-square (r.m.s.) of 0.087 K.

The absorption profile is found by fitting the integrated spectrum with the foreground model and a model for the 21-cm signal simultaneously. The best-fitting 21-cm model yields a symmetric U-shaped absorption profile that is centred at a frequency of  $78 \pm 1$  MHz and has a full-width at half-maximum of  $19^{+4}_{-2}$  MHz, an amplitude of  $0.5^{+0.5}_{-0.2}$  K and a flattening factor of  $\tau = 7^{+5}_{-3}$  (where the bounds provide 99% confidence intervals including estimates of systematic uncertainties; see Methods for model definition). Uncertainties in the parameters of the fitted profile are estimated from statistical uncertainty in the model fits and from systematic differences between the various validation trials that were performed using observations from both instruments and several different data cuts. The 99% confidence intervals that we report are calculated as the outer bounds of (1) the marginalized statistical 99% confidence intervals from fits to the primary dataset and (2) the range of best-fitting values for each parameter across the validation trials. Fitting with both the foreground and 21-cm models lowers the residuals to an r.m.s. of 0.025 K. The fit shown in Fig. 1 has a signal-to-noise ratio of 37, calculated as the best-fitting amplitude of the profile divided by the statistical uncertainty of the amplitude fit, including the covariance between model parameters. Additional analyses of the

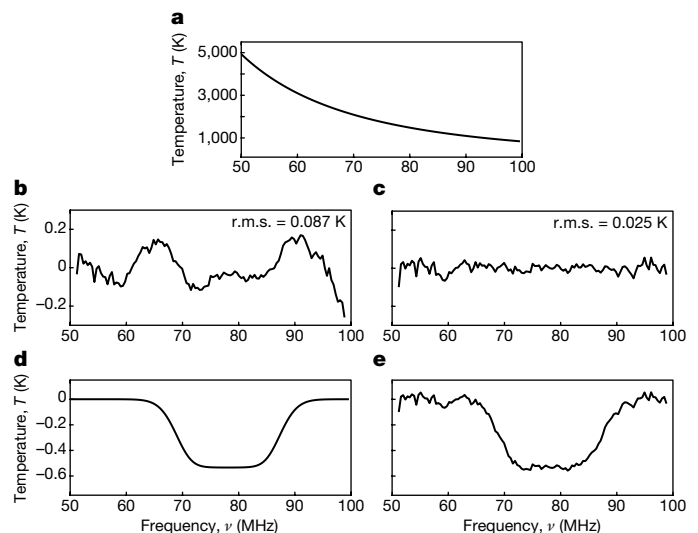


**Figure 1 | Summary of detection.** **a**, Measured spectrum for the reference dataset after filtering for data quality and radio-frequency interference. The spectrum is dominated by Galactic synchrotron emission. **b**, **c**, Residuals after fitting and removing only the foreground model (**b**) or the foreground and 21-cm models (**c**). **d**, Recovered model profile of the 21-cm absorption, with a signal-to-noise ratio of 37, amplitude of 0.53 K, centre frequency of 78.1 MHz and width of 18.7 MHz. **e**, Sum of the 21-cm model (**d**) and its residuals (**c**).

<sup>1</sup>School of Earth and Space Exploration, Arizona State University, Tempe, Arizona 85287, USA. <sup>2</sup>Haystack Observatory, Massachusetts Institute of Technology, Westford, Massachusetts 01886, USA. <sup>3</sup>Center for Astrophysics and Space Astronomy, University of Colorado, Boulder, Colorado 80309, USA. <sup>4</sup>Facultad de Ingeniería, Universidad Católica de la Santísima Concepción, Alonso de Ribera 2850, Concepción, Chile.

**Table 1 | Sensitivity to possible calibration errors**

Error source	Estimated uncertainty	Modelled error level	Recovered amplitude (K)
LNA S11 magnitude	0.1 dB	1.0 dB	0.51
LNA S11 phase (delay)	20 ps	100 ps	0.48
Antenna S11 magnitude	0.02 dB	0.2 dB	0.50
Antenna S11 phase (delay)	20 ps	100 ps	0.48
No loss correction	N/A	N/A	0.51
No beam correction	N/A	N/A	0.48

The estimated uncertainty for each case is based on empirical values from laboratory measurements and repeatability tests. Modelled error levels were chosen conservatively to be five and ten times larger than the estimated uncertainties for the phases and magnitudes, respectively. LNA, low-noise amplifier; S11, input reflection coefficient; N/A, not applicable.

observations using restricted spectral bands yield nearly identical best-fitting absorption profiles, with the highest signal-to-noise ratio reaching 52. In Fig. 2 we show representative cases of these fits.

We performed numerous hardware and processing tests to validate the detection. The 21-cm absorption profile is observed in data that span nearly two years and can be extracted at all local solar times and at all local sidereal times. It is detected by two identically designed instruments operated at the same site and located 150 m apart, and even after several hardware modifications to the instruments, including orthogonal orientations of one of the antennas. Similar results for the absorption profile are obtained by using two independent processing pipelines, which we tested using simulated data. The profile is detected using data processed via two different calibration techniques: absolute calibration and an additional differencing-based post-calibration process that reduces some possible instrumental errors. It is also detected using several sets of calibration solutions derived from multiple laboratory measurements of the receivers and using multiple on-site measurements of the reflection coefficients of the antennas. We modelled the sensitivity of the detection to several possible calibration errors and in all cases recovered profile amplitudes that are within the reported confidence range, as summarized in Table 1. An EDGES high-band instrument operates between 90 MHz and 200 MHz at the same site using a nearly identical receiver and a scaled version of the low-band antennas. It does not produce a similar feature at the scaled frequencies<sup>4</sup>. Analysis of radio-frequency interference in the observations, including in the FM radio band, shows that the absorption profile is inconsistent with typical spectral contributions from these sources.

We are not aware of any alternative astronomical or atmospheric mechanisms that are capable of producing the observed profile. H II regions in the Galaxy have increasing optical depth with wavelength, blocking more background emission at lower frequencies, but they are observed primarily along the Galactic plane and generate monotonic spectral profiles at the observed frequencies. Radio-frequency recombination lines in the Galactic plane create a ‘picket fence’ of narrow absorption lines separated by approximately 0.5 MHz at the observed frequencies<sup>5</sup>, but these lines are easy to identify and filter in the EDGES observations. The Earth’s ionosphere weakly absorbs radio signals at the observed frequencies and emits thermal radiation from hot electrons, but models and observations imply a broadband effect that varies depending on the ionospheric conditions<sup>6,7</sup>, including diurnal changes in the total electron content. This effect is fitted by our foreground model. Molecules of the hydroxyl radical and nitric oxide have spectral lines in the observed band and are present in the atmosphere, but the densities and line strengths are too low to produce substantial absorption.

The 21-cm line has a rest-frame frequency of 1,420 MHz. Expansion of the Universe redshifts the line to the observed band according to  $\nu = 1,420/(1+z)$  MHz, where  $z$  is the redshift, which maps uniquely to the age of the Universe. The observed absorption profile is the continuous superposition of lines from gas across the observed redshift range and cosmological volume; hence, the shape of the profile traces the history of the gas across cosmic time and is not the result of the

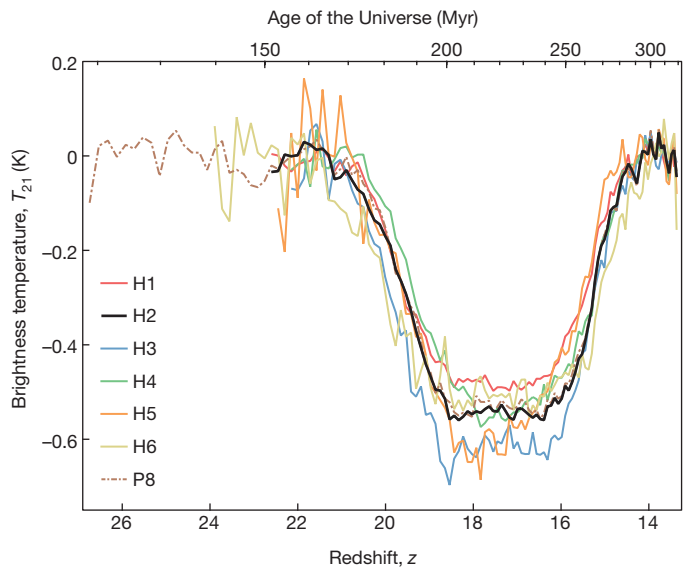


**Figure 2 | Best-fitting 21-cm absorption profiles for each hardware case.** Each profile for the brightness temperature  $T_{21}$  is added to its residuals and plotted against the redshift  $z$  and the corresponding age of the Universe. The thick black line is the model fit for the hardware and analysis configuration with the highest signal-to-noise ratio (equal to 52; H2; see Methods), processed using 60–99 MHz and a four-term polynomial (see equation (2) in Methods) for the foreground model. The thin solid lines are the best fits from each of the other hardware configurations (H1, H3–H6). The dash-dotted line (P8), which extends to  $z > 26$ , is reproduced from Fig. 1e and uses the same data as for the thick black line (H2), but a different foreground model and the full frequency band.

properties of an individual cloud. The observed absorption profile is centred at  $z \approx 17$  and spans approximately  $20 > z > 15$ .

The intensity of the observable 21-cm signal from the early Universe is given as a brightness temperature relative to the microwave background<sup>8</sup>:

$$T_{21}(z) \approx 0.023 \text{ K} \times x_{\text{H}}(z) \left[ \left( \frac{0.15}{\Omega_{\text{m}}} \right) \left( \frac{1+z}{10} \right) \right]^{\frac{1}{2}} \left( \frac{\Omega_{\text{b}} h}{0.02} \right) \left[ 1 - \frac{T_{\text{R}}(z)}{T_{\text{S}}(z)} \right]$$

where  $x_{\text{H}}$  is the fraction of neutral hydrogen,  $\Omega_{\text{m}}$  and  $\Omega_{\text{b}}$  are the matter and baryon densities, respectively, in units of the critical density for a flat universe,  $h$  is the Hubble constant in units of  $100 \text{ km s}^{-1} \text{ Mpc}^{-1}$ ,  $T_{\text{R}}$  is the temperature of the background radiation, usually assumed to be from the background produced by the afterglow of the Big Bang,  $T_{\text{S}}$  is the 21-cm spin temperature that defines the relative population of the hyperfine energy levels, and the factor of 0.023 K comes from atomic-line physics and the average gas density. The spin temperature is affected by the absorption of microwave photons, which couples  $T_{\text{S}}$  to  $T_{\text{R}}$ , as well as by resonant scattering of Lyman- $\alpha$  photons and atomic collisions, both of which couple  $T_{\text{S}}$  to the kinetic temperature of the gas  $T_{\text{G}}$ .

The temperatures of the gas and the background radiation are coupled in the early Universe through Compton scattering. This coupling becomes ineffective in numerical models<sup>9,10</sup> at  $z \approx 150$ , after which primordial gas cools adiabatically. In the absence of stars or non-standard physics, the gas temperature is expected to be 9.3 K at  $z = 20$ , falling to 5.4 K at  $z = 15$ . The radiation temperature decreases more slowly owing to cosmological expansion, following  $T_0(1+z)$  with  $T_0 = 2.725$ , and so is 57.2 K and 43.6 K at the same redshifts, respectively. The spin temperature is initially coupled to the gas temperature as the gas cools below the radiation temperature, but eventually the decreasing density of the gas is insufficient to maintain this coupling and the spin temperature returns to the radiation temperature.

Over time, Lyman- $\alpha$  photons from early stars recouple the spin and gas temperatures<sup>11</sup>, leading to the detected signal. The onset of the observed absorption profile at  $z = 20$  places this epoch at an age of 180 million years, using the Planck 2015 cosmological parameters<sup>12</sup>. For the most extreme case, in which  $T_S$  is fully coupled to  $T_G$ , the gas and radiation temperatures calculated here yield a maximum absorption amplitude of 0.20 K at  $z = 20$ , which increases to 0.23 K at  $z = 15$ .

The presence of stars should eventually halt the cooling of the gas and ultimately heat it, because stellar radiation deposits energy into the gas and Lyman-line cooling has been modelled to be very small for the expected stellar properties<sup>13</sup>. As early stars die, they are expected to leave behind stellar remnants, such as black holes and neutron stars. The accretion disks around these remnants should generate X-rays, further heating the gas. At some point, the gas is expected to become hotter than the background radiation temperature, ending the absorption signal. The  $z = 15$  edge of the observed profile places this transition around 270 million years after the Big Bang.

The ages derived for the events above fall within the range expected from many theoretical models<sup>2</sup>. However, the flattened shape of the observed absorption profile is uncommon in existing models, and could indicate that the initial flux of Lyman- $\alpha$  radiation from early stars was sufficiently large that the spin temperature saturated quickly to the gas temperature. We analysed models that assume a high Lyman- $\alpha$  flux at  $z < 14$  using the EDGES high-band measurements and found a large fraction to be inconsistent with the data<sup>4</sup>.

To produce the best-fitting profile amplitude of 0.5 K, the ratio  $T_R/T_S$  at the centre of the profile must be larger than 15, compared to a maximum of 7 allowed by the gas and radiation temperatures stated above. Even the lower confidence bound of 0.3 K for the observed profile amplitude is roughly 50% larger than the strongest predicted signal. For a standard gas temperature history,  $T_R$  would need to be more than 104 K to yield the best-fitting amplitude at the centre of the profile, whereas for a radiation temperature history given solely by the microwave background,  $T_G$  would need to be less than 3.2 K.

The observed profile amplitude could be explained if the gas and background radiation temperatures decoupled by  $z \approx 250$  rather than  $z \approx 150$ , allowing the gas to begin cooling adiabatically earlier. A residual ionization fraction after the formation of atoms that is less than the expected fraction by nearly an order of magnitude would lead to sufficiently early decoupling. However, cross-validation between numerical models and their consistency with Planck observations suggest that the residual ionization fraction is already known to approximately 1% fractional accuracy.

Considering more exotic scenarios, interactions between dark matter and baryons can explain the observed profile amplitude (by lowering the gas temperature<sup>14</sup>) if the mass of dark-matter particles is below a few gigaelectronvolts and the interaction cross-section is greater than about  $10^{-21} \text{ cm}^2$  (ref. 3). Existing models of other non-standard physics, including dark-matter decay and annihilation<sup>15</sup>, accreting or evaporating primordial black holes<sup>16</sup>, and primordial magnetic fields<sup>17</sup>, all predict increased gas temperatures and are unlikely to account for the observed amplitude. It is possible that some of these sources could also increase  $T_R$  through mechanisms such as synchrotron emission associated with primordial black holes<sup>18</sup> or the relativistic electrons that result from the decay of metastable particles<sup>19</sup>, but it is unclear whether this could compensate for the increased gas temperature. Measurements from ARCADE-2 (ref. 20) suggest an isotropic radio background that cannot be explained by known source populations, but this interpretation is still debated<sup>21</sup> and the unknown sources would need to be present at  $z \approx 20$  to affect the radiation environment relevant to the observed signal.

Although we have performed many tests to be confident that the observed profile is from a global absorption of the microwave background by hydrogen gas in the early Universe, we still seek confirmation observations from other instruments. Several experiments similar to EDGES are underway. Those closest to achieving the performance

required to verify the profile include the Large-Aperture Experiment to Detect the Dark Ages (LEDA)<sup>22</sup>, the Sonda Cosmológica de las Islas para la Detección de Hidrógeno Neutro (SCI-HI)<sup>23</sup>, the Probing Radio Intensity at high  $z$  from Marion (PRIZM) and the Shaped Antenna measurement of the background Radio Spectrum 2 (SARAS 2)<sup>24</sup>. The use of more sophisticated foreground models than we have used could lower the performance requirements of the hardware, and could lead to better profile recovery because low-order (smooth) modes in any fitted profile shape tend to be covariant with our foreground model and so are potentially under-constrained. Singular-value decomposition of training sets constructed from simulated instrument error terms and foreground contributions can produce optimized basis sets for model fitting<sup>25,26</sup>. We plan to apply these techniques to our data processing. The best measurement of the observed profile might ultimately be conducted in space, where the Earth's atmosphere and ionosphere cannot influence the propagation of the astronomical signal, potentially reducing the burden of the foreground model. The measurement could be made from the lunar farside<sup>27</sup>—either on the surface or from an orbit around the Moon—using the Moon as a shield to block FM radio signals and other Earth-based transmitters.

This result should bolster ongoing efforts to detect the statistical properties of spatial fluctuations in the 21-cm signal using interferometric arrays; it provides direct evidence that a signal exists for these telescopes to detect. The Hydrogen Epoch of Reionization Array<sup>28</sup> (HERA) will become operational over the next two years and will be able to characterize the power spectrum of redshifted 21-cm fluctuations between 100 MHz and 200 MHz during the epoch of reionization, when the 21-cm signal should be visible as emission above the background. The operational band of HERA is also expected to be extended to 50 MHz over this time. HERA will probably have sufficient thermal sensitivity to detect any power-spectrum signal associated with the EDGES observed profile and so might be able to validate the absorption signal reported here. But foregrounds have proven to be more challenging for interferometers than expected, and sufficient foreground mitigation to detect the 21-cm power spectrum has yet to be demonstrated by any of the currently operating arrays, including the Low-Frequency Array (LOFAR)<sup>29</sup> and the Murchison Widefield Array (MWA)<sup>30</sup>. Expansion of an existing Long Wavelength Array<sup>31</sup> station would provide the sensitivity necessary to pursue power-spectrum detection. When constructed, the Square Kilometre Array (SKA) Low-Frequency Aperture Array (<https://www.skatelescope.org>) should be able to detect the power spectrum associated with the absorption profile reported here and, eventually, to image the 21-cm signal.

**Online Content** Methods, along with any additional Extended Data display items and Source Data, are available in the online version of the paper; references unique to these sections appear only in the online paper.

**Received 13 September 2017; accepted 24 January 2018.**

1. Pritchard, J. R. & Loeb, A. 21 cm cosmology in the 21st century. *Rep. Prog. Phys.* **75**, 086901 (2012).
2. Cohen, A., Fialkov, A., Barkana, R. & Loeb, M. Charting the parameter space of the global 21-cm signal. *Mon. Not. R. Astron. Soc.* **472**, 1915–1931 (2017).
3. Barkana, R. Possible interaction between baryons and dark-matter particles revealed by the first stars. *Nature* **555**, <https://doi.org/10.1038/nature25791> (2018).
4. Monsalve, R. A., Rogers, A. E. E., Bowman, J. D. & Mozdzen, T. J. Results from EDGES high-band. I. Constraints on phenomenological models for the global 21 cm signal. *Astrophys. J.* **847**, 64 (2017).
5. Alves, M. I. R. et al. The HIPASS survey of the Galactic plane in radio recombination lines. *Mon. Not. R. Astron. Soc.* **450**, 2025–2042 (2015).
6. Rogers, A. E. E., Bowman, J. D., Vierinen, J., Monsalve, R. A. & Mozdzen, T. Radiometric measurements of electron temperature and opacity of ionospheric perturbations. *Radio Sci.* **50**, 130–137 (2015).
7. Sokolowski, M. et al. The impact of the ionosphere on ground-based detection of the global epoch of reionization signal. *Astrophys. J.* **813**, 18 (2015).
8. Zaldarriaga, M., Furlanetto, S. R. & Hernquist, L. 21 centimeter fluctuations from cosmic gas at high redshifts. *Astrophys. J.* **608**, 622–635 (2004).
9. Ali-Haïmoud, Y. & Hirata, C. M. HyRec: a fast and highly accurate primordial hydrogen and helium recombination code. *Phys. Rev. D* **83**, 043513 (2011).



10. Shaw, J. R. & Chluba, J. Precise cosmological parameter estimation using COSMOREC. *Mon. Not. R. Astron. Soc.* **415**, 1343–1354 (2011).
11. Furlanetto, S. R. The global 21-centimeter background from high redshifts. *Mon. Not. R. Astron. Soc.* **371**, 867–878 (2006).
12. Planck Collaboration. Planck 2015 results. XIII. Cosmological parameters. *Astron. Astrophys.* **594**, A13 (2016).
13. Chen, X. & Miralda-Escude, J. The spin-kinetic temperature coupling and the heating rate due to Ly $\alpha$  scattering before reionization: predictions for 21 centimeter emission and absorption. *Astrophys. J.* **602**, 1–11 (2004).
14. Tashiro, H., Kadota, K. & Silk, J. Effects of dark matter-baryon scattering on redshifted 21 cm signals. *Phys. Rev. D* **90**, 083522 (2014).
15. Lopez-Honorez, L., Mena, O., Molin  ,   ., Palomares-Ruiz, S. & Vincent, A. C. The 21 cm signal and the interplay between dark matter annihilations and astrophysical processes. *J. Cosmol. Astropart. Phys.* **8**, 4 (2016).
16. Tashiro, H. & Sugiyama, N. The effect of primordial black holes on 21-cm fluctuations. *Mon. Not. R. Astron. Soc.* **435**, 3001–3008 (2013).
17. Schleicher, D. R. G., Banerjee, R. & Klessen, R. S. Influence of primordial magnetic fields on 21 cm emission. *Astrophys. J.* **692**, 236–245 (2009).
18. Biermann, P. L. *et al.* Cosmic backgrounds due to the formation of the first generation of supermassive black holes. *Mon. Not. R. Astron. Soc.* **441**, 1147–1156 (2014).
19. Cline, J. M. & Vincent, A. C. Cosmological origin of anomalous radio background. *J. Cosmol. Astropart. Phys.* **2**, 11 (2013).
20. Seiffert, M. *et al.* Interpretation of the Arcade 2 absolute sky brightness measurement. *Astrophys. J.* **734**, 6 (2011).
21. Vernstrom, T., Norris, R. P., Scott, D. & Wall, J. V. The deep diffuse extragalactic radio sky at 1.75 GHz. *Mon. Not. R. Astron. Soc.* **447**, 2243–2260 (2015).
22. Bernardi, G. *et al.* Bayesian constraints on the global 21-cm signal from the cosmic dawn. *Mon. Not. R. Astron. Soc.* **461**, 2847–2855 (2016).
23. Voytek, T. C., Natarajan, A., J  uregui Garc  a, J. M., Peterson, J. B. & L  pez-Cruz, O. Probing the dark ages at  $z \sim 20$ : the SCL-HI 21 cm all-sky spectrum experiment. *Astrophys. J.* **782**, L9 (2014).
24. Singh, S. *et al.* First results on the epoch of reionization from first light with SARAS 2. *Astrophys. J.* **845**, L12 (2017).
25. Switzer, E. R. & Liu, A. Erasing the variable: empirical foreground discovery for global 21 cm spectrum experiments. *Astrophys. J.* **793**, 102 (2014).
26. Vedantham, H. K. *et al.* Chromatic effects in the 21 cm global signal from the cosmic dawn. *Mon. Not. R. Astron. Soc.* **437**, 1056–1069 (2014).
27. Burns, J. O. *et al.* A space-based observational strategy for characterizing the first stars and galaxies using the redshifted 21 cm global spectrum. *Astrophys. J.* **844**, 33 (2017).
28. DeBoer, D. R. *et al.* Hydrogen Epoch of Reionization Array (HERA). *Publ. Astron. Soc. Pac.* **129**, 045001 (2017).
29. Patil, A. H. *et al.* Upper limits on the 21 cm epoch of reionization power spectrum from one night with LOFAR. *Astrophys. J.* **838**, 65 (2017).
30. Beardsley, A. P. *et al.* First season MWA EoR power spectrum results at redshift 7. *Astrophys. J.* **833**, 102 (2016).
31. Dowell, J., Taylor, G. B., Schinzel, F. K., Kassim, N. E. & Stovall, K. The LWA1 low frequency sky survey. *Mon. Not. R. Astron. Soc.* **469**, 4537–4550 (2017).

**Acknowledgements** We thank CSIRO for providing site infrastructure and access to facilities. We thank the MRO Support Facility team, especially M. Reay, L. Puls, J. Morris, S. Jackson, B. Hiscock and K. Ferguson. We thank C. Bowman, D. Cele, C. Eckert, L. Johnson, M. Goodrich, H. Mani, J. Traffie and K. Wilson for instrument contributions. We thank R. Barkana for theory contributions and G. Holder, T. Vachaspati, C. Hirata and J. Chluba for exchanges. We thank C. Lonsdale, H. Johnson, J. Hewitt and J. Burns. We thank C. Halleen and M. Halleen for site and logistical support. This work was supported by the NSF through awards AST-0905990, AST-1207761 and AST-1609450. R.A.M. acknowledges support from the NASA Ames Research Center (NNX16AF59G) and the NASA Solar System Exploration Research Virtual Institute (80ARCO17M0006). This work makes use of the Murchison Radio-astronomy Observatory. We acknowledge the Wajarri Yamatji people as the traditional owners of the site of the observatory.

**Author Contributions** J.D.B., R.A.M. and A.E.E.R. contributed to all activities. N.M. and T.J.M. modelled instrument properties, performed laboratory calibrations and contributed to the preparation of the manuscript.

**Author Information** Reprints and permissions information is available at [www.nature.com/reprints](http://www.nature.com/reprints). The authors declare no competing financial interests. Readers are welcome to comment on the online version of the paper. Publisher's note: Springer Nature remains neutral with regard to jurisdictional claims in published maps and institutional affiliations. Correspondence and requests for materials should be addressed to J.D.B. ([judd.bowman@asu.edu](mailto:judd.bowman@asu.edu)).

**Reviewer Information** *Nature* thanks S. Weinreb and the other anonymous reviewer(s) for their contribution to the peer review of this work.

## METHODS

**Instrument.** The EDGES experiment is located at the Murchison Radio-astronomy Observatory (MRO) in Western Australia (26.72° S, 116.61° E), which is the same radio-quiet<sup>32</sup> site used by the Australian SKA precursor, the Murchison Widefield Array and the planned SKA Low-Frequency Aperture Array. An early version of EDGES placed an empirical lower limit on the duration of the epoch of reionization<sup>33</sup>. EDGES currently consists of three instruments: a high-band instrument<sup>4,34,35</sup> that is sensitive to 90–200 MHz ( $14 > z > 6$ ) and two low-band instruments (low-1 and low-2) that operate over the range 50–100 MHz ( $27 > z > 13$ ). Each instrument yields spectra with 6.1-kHz resolution. In each instrument, sky radiation is collected by a wideband dipole-like antenna that consists of two rectangular metal panels mounted horizontally above a metal ground plane. Similar compact dipole antennas are used elsewhere in radio astronomy<sup>36,37</sup>. A receiver is installed underneath the ground plane and a balun<sup>38</sup> is used to guide radiation from the antenna panels to the receiver. A rectangular shroud surrounds the base of the balun to shield the vertical currents in the balun tubes, which are strongest at the base. This lowers the gain towards the horizon owing to the vertical currents.

Extended Data Fig. 1 shows a block diagram of the system. A mechanical input switch at the front of the receiver enables the antenna to be connected to a remote vector network analyser (VNA) to measure the antenna reflection coefficients accurately or to be connected to the primary receiver path to measure the sky noise spectrum. When measuring the sky noise spectrum a second mechanical switch connects the low-noise amplifier (LNA) to the antenna or to a 26-dB attenuator, which acts as a load or a well matched noise source, depending on the state of the electrical switch on the noise source. This performs a three-position switching operation<sup>39</sup> between ambient and ‘hot’ internal noise sources and the antenna, which is needed to provide the first stage of processing discussed below. After the LNA and post-amplifier, another noise source is used to inject noise at less than 45 MHz. This ‘out of band’ conditioning improves the linearity and dynamic range of the analogue-to-digital converter (ADC), which are needed for the accurate cancellation of the receiver bandpass that is afforded by the three-position switching. A thermoelectric system maintains a constant temperature in the receiver in the field and in the laboratory. The system mitigates against radio-frequency interference (RFI) using designs and analysis strategies adapted from the Deuterium Array<sup>40</sup>. Similar approaches to instrument design are used for SARAS 2 (ref. 41) and LEDA<sup>42</sup>.

The design of the low-band instrument differs from the published descriptions of the design of the high-band instrument only by the following. First, a 3-dB attenuator is added within the LNA before the pseudomorphic high-electron-mobility transistor at the input. The attenuator improves the LNA impedance match and thereby reduces the sensitivity to measurement errors of the LNA and antenna reflection coefficients, especially to errors in the reflection phase, while adding only a small amount of noise compared with the sky noise. Larger values of attenuation would begin to add substantial noise at 100 MHz. Second, a scaled antenna is used that is precisely double the size of the antenna of the high-band instrument. Third, a larger ground plane is used. Each ground plane of the low-band instrument consists of a  $2 \text{ m} \times 2 \text{ m}$  solid metal central assembly surrounded by metal mesh that spans  $30 \text{ m} \times 30 \text{ m}$ , with the outer 5 m shaped as saw-tooth perforated edges. Low-1 was initially operated with a  $10 \text{ m} \times 10 \text{ m}$  ground plane and later extended to full size. The full-size  $30 \text{ m} \times 30 \text{ m}$  ground plane reduces the chromaticity of the beam and makes it less sensitive to conditions of the soil. Extended Data Fig. 2 shows the low-1 and low-2 antennas, Extended Data Fig. 3 the measured reflection coefficients and Extended Data Fig. 4 cuts through the model of the antenna beam pattern.

**Calibration.** We implement end-to-end absolute calibration for the low-band instruments following the techniques developed for the high-band instrument<sup>34,43</sup>. The calibration procedure involves taking reference spectra in the laboratory with the receiver connected to hot and ambient loads and to open and shorted cables. Similar techniques are used in other microwave measurements<sup>44,45</sup>. Reflection coefficient measurements using a VNA are acquired for the calibration sources and the LNA. The input connection to the receiver box provides the reference plane for all VNA measurements. To correct for the losses in the hot load used in the laboratory for calibration, full scattering parameters are measured for the short cable from the heated resistor in the hot load. The accuracy of scattering parameter measurements is improved by accounting for the actual resistance of the 50- $\Omega$  load used for VNA calibration and the added inductance in the load due to skin effects<sup>46</sup> in the few millimetres of transmission line between its internal termination and the reference plane<sup>47</sup>.

The calibration spectra and reflection coefficient measurements acquired in the laboratory are used to solve for the free parameters<sup>34</sup> in the equations that account for the impedance mismatches between the receiver and the antenna and for the

correlated and uncorrelated LNA noise waves. Laboratory calibration is performed with the receiver temperature controlled to the default 25°C, and at 15°C and 35°C to assess the thermal dependence of the calibration parameters. Extended Data Fig. 5 shows calibration parameter solutions for both receivers.

Following calibration in the laboratory, a test is performed by measuring the spectrum of an approximately 300 K passive load with deliberate impedance mismatch that approximately mimics the reflection from the antenna in magnitude and phase. We call this device an ‘artificial antenna simulator’. The reflection coefficient of the antenna simulator is measured and applied to yield calibrated integrated spectra. Extended Data Fig. 3 shows measured reflection coefficients for the artificial antenna simulator. Once corrected, the integrated spectra are expected to be spectrally flat, with a noise temperature that matches the physical temperature of the passive load. The flatness of an integrated spectrum is quantified through the r.m.s. of the residuals after subtracting a constant term. The typical r.m.s. of the residuals is 0.025 K over the range 50–100 MHz. If a three-term polynomial (equation (2) with  $N = 3$ ) is subtracted, then the residuals decrease to about 0.015 K and are limited by integration time.

A second test of the calibration is performed by measuring the spectrum of a noise source followed by a filter and an approximately 3-m cable that adds about 30 ns of two-way delay. The device yields a spectrum that is similar in shape to the sky foreground with a strength of about 10,000 K (seven times larger than the typical sky temperature observed by EDGES) at 75 MHz and has a reflection coefficient of  $-6 \text{ dB}$  in magnitude with a phase slope similar to that of the antenna. Typical residuals are less than 300 mK after subtracting a five-term polynomial (equation (2)) and are limited by integration time. Assuming any residuals scale with input power, this value corresponds to residuals of 45 mK at the typical observed sky temperature. This test is more sensitive than the passive simulator, especially to errors in the measurements of the reflection coefficient, because the signal is 33 times stronger than that of the approximately 300-K load and because the magnitude of the reflection of this simulator is larger than that of the passive simulator and of the real antenna.

Losses in the balun and losses due to the finite ground plane are corrected for during data processing using models. The balun-loss model is validated against scattering parameter measurements. Frequency-dependent beam effects are compensated for by modelling and subtracting the spectral structure using electromagnetic beam models and a diffuse sky map template<sup>35</sup>. The nominal beam model accounts for the finite metal ground plane over soil with a relative permittivity of 3.5 and conductivity of  $2 \times 10^{-2} \text{ S m}^{-1}$  (ref. 48). The sky template is produced by extrapolating the 408-MHz all-sky radio map<sup>49</sup> to the observed frequencies using a spectral index in brightness temperature of  $-2.5$  (refs 35, 43).

**Data and processing.** Examples of raw and processed data are shown in Extended Data Fig. 6. Data processing involves three primary stages. In the first stage, three raw spectra that have each been accumulated for 13 s from the antenna input and two internal reference noise sources are converted into a single partially calibrated spectrum<sup>39</sup>. Individual 6.1-kHz channels above a fixed power threshold are assigned zero weight to remove RFI. The threshold is normally set at three times the r.m.s. of the residuals after subtracting a constant and a slope in a sliding 256-spectral-channel window. Similarly, any partially calibrated spectrum with an average power above that expected from the sky or with large residuals is discarded. A weighted average of many successive spectra is taken, typically over several hours. Outlier channels after a Fourier series fit to the entire accumulated spectrum are again assigned zero weight. This second pass assigns zero weight to lower levels of RFI and broader RFI signals than does the initial pass.

In the second stage of processing, the partially calibrated spectra are fully calibrated using the calibration parameters from the laboratory and the antenna reflection coefficient measurements taken periodically in the field. Beam-chromaticity corrections are applied after averaging the model over the same range of local sidereal times as for the spectra. The spectra are then corrected for the balun and ground-plane loss and output with a typical smoothing to spectral bins with 390.6-kHz resolution.

In the third stage of processing, spectra for each block of local sidereal time of several hours within each day are fitted with a foreground model (see below for description of models). An r.m.s. value of the residuals is computed for each block and blocks above a selected threshold are discarded, typically because of broadband RFI—or solar activity in daytime data—that was not detected in the earlier processing stages. A weighted average is then taken of the accepted blocks and a weighted least-squares solution is determined using a foreground model along with the model that represents the 21-cm absorption signal. Extended Data Fig. 7 shows the final weights for each spectral bin, equivalent to the RFI occupancy.

The observations used for the primary analysis presented here are from low-1, spanning 2016 day 252 through to 2017 day 94 (configuration H2 below). The data are filtered to retain only local Galactic hour angles (GHA) of 6–18 h; GHA is equivalent to the local sidereal time offset by 17.75 h.

**Parameter estimation.** The polynomial foreground model used for the analysis presented in Fig. 1 is physically motivated, with five terms based on the known spectral properties of the Galactic synchrotron spectrum and Earth's ionosphere<sup>5,50</sup>:

$$T_F(\nu) \approx a_0 \left( \frac{\nu}{\nu_c} \right)^{-2.5} + a_1 \left( \frac{\nu}{\nu_c} \right)^{-2.5} \log \left( \frac{\nu}{\nu_c} \right) + a_2 \left( \frac{\nu}{\nu_c} \right)^{-2.5} \left[ \log \left( \frac{\nu}{\nu_c} \right) \right]^2 + a_3 \left( \frac{\nu}{\nu_c} \right)^{-4.5} + a_4 \left( \frac{\nu}{\nu_c} \right)^{-2} \quad (1)$$

where  $T_F(\nu)$  is the brightness temperature of the foreground emission,  $\nu$  is the frequency,  $\nu_c$  is the centre frequency of the observed band and the coefficients  $a_n$  are fitted to the data. The above function is a linear approximation, centred on  $\nu_c$ , to

$$T_F(\nu) = b_0 \left( \frac{\nu}{\nu_c} \right)^{-2.5+b_1+b_2 \log(\nu/\nu_c)} e^{-b_3(\nu/\nu_c)^{-2}} + b_4 \left( \frac{\nu}{\nu_c} \right)^{-2}$$

which is connected directly to the physics of the foreground and the ionosphere. The factor of  $-2.5$  in the first exponent is the typical power-law spectral index of the foreground,  $b_0$  is an overall foreground scale factor,  $b_1$  allows for a correction to the typical spectral index of the foreground (which varies by roughly 0.1 across the sky) and  $b_2$  captures any contributions from a higher-order foreground spectral term<sup>51,52</sup>. Ionospheric contributions are contained in  $b_3$  and  $b_4$ , which allow for the ionospheric absorption of the foreground and emission from hot electrons in the ionosphere, respectively. This model can also partially capture some instrumental effects, such as additional spectral structure from chromatic beams or small errors in calibration.

We also use a more general polynomial model in many of our trials that enables us to explore signal recovery with varying numbers of polynomial terms:

$$T_F(\nu) = \sum_{n=0}^{N-1} a_n \nu^{n-2.5} \quad (2)$$

where  $N$  is the number of terms and the coefficients  $a_n$  are again fitted to the data. As with the physical model, the  $-2.5$  in the exponent makes it easier for the model to match the foreground spectrum. Both foreground models yield consistent absorption profile results.

The 21-cm absorption profile is modelled as a flattened Gaussian:

$$T_{21}(\nu) = -A \left( \frac{1 - e^{-\tau e^B}}{1 - e^{-\tau}} \right)$$

where

$$B = \frac{4(\nu - \nu_0)^2}{w^2} \log \left[ -\frac{1}{\tau} \log \left( \frac{1 + e^{-\tau}}{2} \right) \right]$$

and  $A$  is the absorption amplitude,  $\nu_0$  is the centre frequency,  $w$  is the full-width at half-maximum and  $\tau$  is a flattening factor. This model is not a description of the physics that creates the 21-cm absorption profile, but rather is a suitable functional form to capture the basic shape of the profile. Extended Data Fig. 8 shows the best-fitting profile and residuals from fits by the two foreground models.

We report parameter fits from a gridded search over the parameters  $\nu_0$ ,  $w$  and  $\tau$  in the 21-cm model. For each step in the grid, we conduct a linear weighted least-squares fit, solving simultaneously for the foreground coefficients and the amplitude of the absorption profile. The best-fitting absorption profile maximizes the signal-to-noise ratio in the gridded search. The uncertainty in the amplitude fit accounts for covariance between the foreground coefficients and the amplitude of the profile and for noise.

Fitting both foreground and 21-cm models simultaneously yields residuals that decrease with integration time with an approximately noise-like ( $1/\sqrt{t}$ ) trend for the duration of the observation, whereas fitting only the foreground model yields residuals that decrease with time for the first approximately 10% of the integration and then saturate, as shown in Extended Data Fig. 9.

We also performed a Markov chain Monte Carlo (MCMC) analysis (Extended Data Fig. 10) for the H2 case using a five-term polynomial (equation (2)) for the foreground model and a subset of the band covering 60–94 MHz. The amplitude parameter is most covariant with the flattening. The 99% statistical confidence intervals on the four 21-cm model parameters are:  $A = 0.52^{+0.42}_{-0.18}$  K,  $\nu_0 = 78.3^{+0.2}_{-0.3}$  MHz,  $w = 20.7^{+0.8}_{-2.5}$  MHz and  $\tau = 6.5^{+5.6}_{-2.5}$ . These intervals do not include any systematic error from differences across the hardware configurations and processing trials. When the flattening parameter is fixed to  $\tau = 7$ , statistical uncertainty in the 21-cm model amplitude fit is reduced to approximately  $\pm 0.02$  K.

Extended Data Table 1 shows that the various hardware configurations and processing trials with fixed  $\tau = 7$  yield best-fitting parameter ranges of  $0.37 \text{ K} < A < 0.67 \text{ K}$ ,  $77.4 \text{ MHz} < \nu_0 < 78.5 \text{ MHz}$  and  $17.0 \text{ MHz} < w < 22.8 \text{ MHz}$ . This systematic variation is probably due to the limited data in some of the configurations, small calibration errors and residual chromatic beam effects, and potentially to structure in the Galactic foreground that increases when the Galactic plane is overhead. For each parameter, taking the outer bounds of the statistical confidence ranges from the comprehensive MCMC analysis for H2 and the best-fitting variations between validation trials in Extended Data Table 1 yields the estimate of the 99% confidence intervals that we report in the main text.

**Verification tests.** Here we list the tests that we performed to verify the detection. The absorption profile is detected from data obtained in the following hardware configurations: H1, low-1 with  $10 \text{ m} \times 10 \text{ m}$  ground plane; H2, low-1 with  $30 \text{ m} \times 30 \text{ m}$  ground plane; H3, low-1 with  $30 \text{ m} \times 30 \text{ m}$  ground plane and recalibrated receiver; H4, low-2 with north–south dipole orientation; H5, low-2 with east–west dipole orientation; and H6, low-2 with east–west dipole orientation and the balun shield removed to check for any resonance that might result from a slot antenna being formed in the joint between the two halves of the shield.

The absorption profile is detected in data processed with the following configurations: P1, all hardware cases, using two independent processing pipelines; P2, all hardware cases, divided into temporal subsets; P3, all hardware cases, with chromatic beam corrections on or off; P4, all hardware cases, with ground loss and balun loss corrections on or off; P5, all hardware cases, calibrated with four different antenna reflection coefficient measurements; P6, all hardware cases, using a four-term foreground model (equation (2)) over the frequency range 60–99 MHz; P7, all hardware cases, using a five-term foreground model (equation (2)) over the frequency range 60–99 MHz; P8, all hardware cases, using the physical foreground model (equation (1)) over the frequency range 51–99 MHz; P9, all hardware configurations, using various additional combinations of four-, five-, and six-term foreground models (equation (2)) and various frequency ranges; P10, H2 binned by local sidereal time/GHA; P11, H2 binned by UTC; P12, H2 binned by buried conduit temperature as a proxy for the ambient temperature at the receiver and the temperature of the cable that connects the receiver frontend under the antenna to the backend in the control hut; P13, H2 binned by Sun above or below the horizon; P14, H2 binned by Moon above or below the horizon; P15, H2 with added post-calibration calculated by subtracting scaled Galaxy-up spectra from Galaxy-down spectra; P16, H2 calibrated with low-2 solutions; P17, H4 calibrated with laboratory measurements at 15 °C and 35 °C; and P18, H2 and H3 calibrated with laboratory measurements spanning two years.

Extended Data Table 1 lists the properties of the profile for each of the hardware configurations (H1–H6) with the standard processing configuration (P6); Fig. 2 illustrates the corresponding best-fitting profiles. The variations in signal-to-noise ratio between the configurations are largely explained by differences in the total integration time for each configuration, except for H1, which was limited by its ground-plane performance. We acquired the most data in configuration H1, with approximately 11 months of observations, followed by H2 with 6 months. The other configurations were each operated for 1–2 months before the analysis presented here was performed. Extended Data Table 2 lists the profile amplitudes for data binned by GHA for both processing pipelines used in configuration P1.

The following additional verification tests were performed to check specific aspects of the instrument, laboratory calibration and processing pipelines. (1) We processed simulated data and recovered injected profiles. (2) We searched for a similar profile at the scaled frequencies in high-band data and found no corresponding profile. (3) We measured the antenna reflection coefficients of low-2 with the VNA connected to its receiver via a short 2-m cable and found nearly identical results to when the 100-m cable was used (under normal operation). (4) We acquired *in situ* reflection coefficient measurements that matched our model predictions of the low-2 balun with the antenna terminal shorted and open; this was done to verify our model for the balun loss. (5) We tested the performance of the receivers in the laboratory using artificial antenna sources connected to the receivers directly, as described above. (6) We cross-checked our beam models using three electromagnetic numerical solvers: CST, FEKO and HFSS. Although no beam model is required to detect the profile because the EDGES antenna is designed to be largely achromatic, we performed the cross-check because we apply beam corrections in the primary analysis.

**Sensitivity to systematic errors.** Here we discuss in more detail several primary categories of potential systematic errors and the validation steps that we performed. *Beam and sky effects.* Beam chromaticity is larger than can be accounted for with electromagnetic models of the antenna on an infinite ground plane<sup>53</sup>. For both ground plane sizes, the r.m.s. of the residuals to low-order foreground polynomial model fits of the data matched electromagnetic modelling when the model accounted for the finite ground-plane size and included the effects of the dielectric



constant and the conductivity of the soil under the ground plane. The residual structures themselves matched qualitatively.

Comparing electromagnetic solvers for beam models, we found that for infinite ground-plane models the change in the absolute gain of the beam with frequency at every viewing angle ( $\theta, \phi$ ) was within  $\pm 0.006$  between solvers and that residuals after foreground fits to simulated spectra were within a factor of two. For models with finite ground planes and real soil properties, we found that correcting H1 data using beam models from FEKO and HFSS in integral solver modes resulted in nearly identical 21-cm model parameter values, although using an HFSS model for the larger ground plane in H2 resulted in a fit to the profile that had a lower signal-to-noise ratio than when using the FEKO model, but still a higher signal-to-noise ratio than when no beam correction was used (see Extended Data Table 1).

The low-2 instrument was deployed 100 m west of the control hut, whereas the low-1 instrument was 50 m east of the hut. In the east–west antenna orientation, the low-2 dipole-response null was aimed approximately at the control hut and the beam pattern on the sky was rotated relative to north–south. Obtaining consistent absorption profiles with the two sizes of low-1 ground planes (H1 versus H2 or H3) and with both low-2 antenna orientations (H4 versus H5 or H6) suggests that beam effects are not responsible for the profile, while obtaining the same results from both low-2 antenna orientations also disfavours polarized sky emission as a possible source of the profile. Obtaining consistent absorption profiles with the low-1 and low-2 instruments at different distances from the control hut and with both low-2 antenna orientations suggests that it is unlikely that the observed profile is produced by reflections of sky noise from the control hut or other surrounding objects or caused by RFI from the hut. Our understanding of hut reflections is further validated by the appearance of small sinusoidal ripples after subtracting a nine-term foreground model (equation (2)) from the low-1 spectra at GHA 20. These ripples are consistent with models of hut reflections and not evident at other GHAs or in the low-2 data.

**Gain and loss errors.** Many possible instrumental systematic errors and atmospheric effects that could potentially mimic the observed absorption profile are due to inaccurate or unaccounted for gains or losses in the propagation path within the instrument or Earth's atmosphere. If present, these effects would be proportional to the total sky noise power entering the system. The total sky noise power received by EDGES varies by a factor of three over GHA. If the observed absorption profile were due to gain or loss errors, the amplitude of the profile would be expected to vary in GHA proportional to the sky noise.

We tested for these errors by fitting for the absorption profile in observations binned by GHA in 4-h and 6-h blocks using H2 data. The test is complicated by the increase in chromatic-beam effects in spectra when the sky noise power is large owing to the presence of the Galactic plane in the antenna beam. We compensated for this by increasing the foreground model to up to six polynomial terms for the GHA analysis and using the FEKO antenna beam model to correct for beam effects. As evident in Extended Data Table 2, the best-fitting amplitudes averaged over each GHA bin are consistent within the reported uncertainties and exhibit no substantial correlation with sky noise power. The same test performed using a four-term polynomial foreground model (equation (2)) did yield variations with GHA, as did tests performed on data from low-1 with the  $10\text{ m} \times 10\text{ m}$  ground plane. We attribute the failure of these two cases to beam effects and possible foreground structure. Other cases tested had insufficient data for conclusive results, but did not show any correlation with the total sky noise power.

The artificial antenna measurements described in Methods section 'Calibration' provide verification of the smooth passband of the receiver after calibration. Because we observe the 0.5-K signature for all foreground conditions, including low foregrounds of about 1,500 K at about 78 MHz, if the observed profile were an instrumental artefact due to an error in gain of the receiver, then we would expect to see a scaled version of the profile with an amplitude of  $0.5\text{ K} \times (300\text{ K}/1,500\text{ K}) = 0.1\text{ K}$  when measuring the approximately 300-K artificial antenna. Instead, we see a smooth spectrum structure at the approximately 0.025-K level. With the 10,000-K artificial antenna, we would expect to see a 3.3-K profile that yields 0.5-K residuals after subtracting a five-term polynomial fit (equation (2)); instead we find residuals that are less than 0.3 K.

Receiver calibration errors are disfavoured as the source of the observed profile. Three verification tests were performed to investigate this possibility specifically by processing data with inaccurate calibration parameter solutions. First, in verification test P18 we processed H2 and H3 datasets using each of the three low-1 receiver calibration solutions shown in Extended Data Fig. 5a–g. The observed profile was detected in each case, indicating that the detection is robust to these small drifts in the calibration parameters over the two-year period spanning the use of the low-1 receiver. Second, in verification test P17 we processed H4 observations using the calibration solutions derived from laboratory measurements acquired with the receiver temperature held at both  $15^\circ\text{C}$  and  $35^\circ\text{C}$ , even though it was

controlled to  $25^\circ\text{C}$  for all observations. The profile was recovered even for these larger calibration differences and so we infer that the detection is robust to the much smaller variations of typically  $0.1^\circ\text{C}$  in the receiver temperature around its set point during operation. Third, as a final check of the receiver properties, in P16 we calibrated the H2 dataset from low-1 using the receiver calibration solutions derived for low-2. The profile was recovered using a seven-term foreground model (equation (2)) over the range 53–99 MHz. This provides evidence that both receivers have generally similar properties and spectrally smooth responses; otherwise, we would not expect the calibration solutions to be interchangeable in this manner.

**RFI and FM radio.** RFI is found to be minimal in EDGES low-band measurements. We rule out locally generated broadband RFI from the control hut and a nearby ASKAP dish (more than 150 m away) as the source of the profile because of the consistent profiles observed by both instruments and both low-2 antenna orientations, as noted above. There are no licensed digital TV transmitters in Australia below 174 MHz (<https://www.acma.gov.au>, ITU RCC-06). We analysed observations and rule out the FM radio band, which spans 87.5–108 MHz, as the cause of the high-frequency edge of the observed profile. FM transmissions within about 3,000 km of the MRO could be scattered from aeroplanes or from meteors that burn up at an altitude of about 100 km in the mesosphere. Inspection of channels removed by our RFI detection algorithms and of spectral residuals using the instrument's raw 6.1-kHz resolution, which oversamples the minimum 50-kHz spacing of the FM channel centres, shows that these signals are sparse and transient and show up after removal as mostly zero-weighted channels. More persistent worldwide FM signals reflected from the Moon have been measured<sup>54</sup> from the MRO with flux density about 100 Jy. We find evidence for a sharp step of around 0.05 K at 87.5 MHz in our binned spectra when the Moon is above  $45^\circ$  elevation, which can be eliminated by using only data from when the Moon is below the horizon.

**Atmospheric molecular lines.** Atmospheric nitrous oxide line absorption was modelled using a line strength of  $10^{-12.7}\text{ nm}^2\text{ MHz}$  at 300 K based on values from the spectral line catalogue maintained by the Molecular Spectroscopy Team at the Jet Propulsion Laboratory and an abundance of 70 parts per billion. We assumed a 3,000-K sky-noise temperature and a line-of-sight path through the atmosphere at  $8^\circ$  elevation and integrated over the altitude range 10–120 km. We find up to 0.001 mK of absorption per line. With approximately 100 individual lines between 50 MHz and 100 MHz, we conservatively estimate a maximum possible contribution of 0.1 mK.

**Gas temperature and residual ionization fraction.** For the gas thermal calculations, we used CosmoRec<sup>10</sup> to model the evolution of the electron temperature and residual ionization fraction for  $z < 3,000$ . We verified the output against solutions to equations<sup>55</sup> for the dominant contributions to the electron temperature evolution of adiabatic expansion and Compton scattering. We assume that the gas temperature is in equilibrium with the electron temperature. To determine the residual ionization fraction that is required to produce sufficiently cold gas to account for the observed profile amplitude, we modelled a partial ionization step function in redshift. We used the ionization fraction from CosmoRec for redshifts above the transition and a constant final ionization fraction below the transition. We performed a grid search in transition redshift and final ionization fraction to identify the lowest transition redshift for the largest final ionization fraction that results in the required gas temperature. We found that a final ionization fraction of around  $3 \times 10^{-5}$  reached by  $z \approx 500$  would be sufficient to produce the required gas temperature. This is nearly an order of magnitude lower than the expected ionization fraction of around  $2 \times 10^{-4}$  at similar ages from CosmoRec.

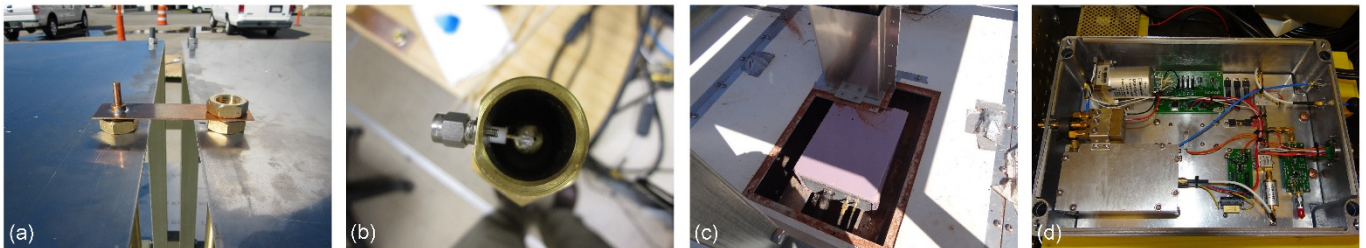
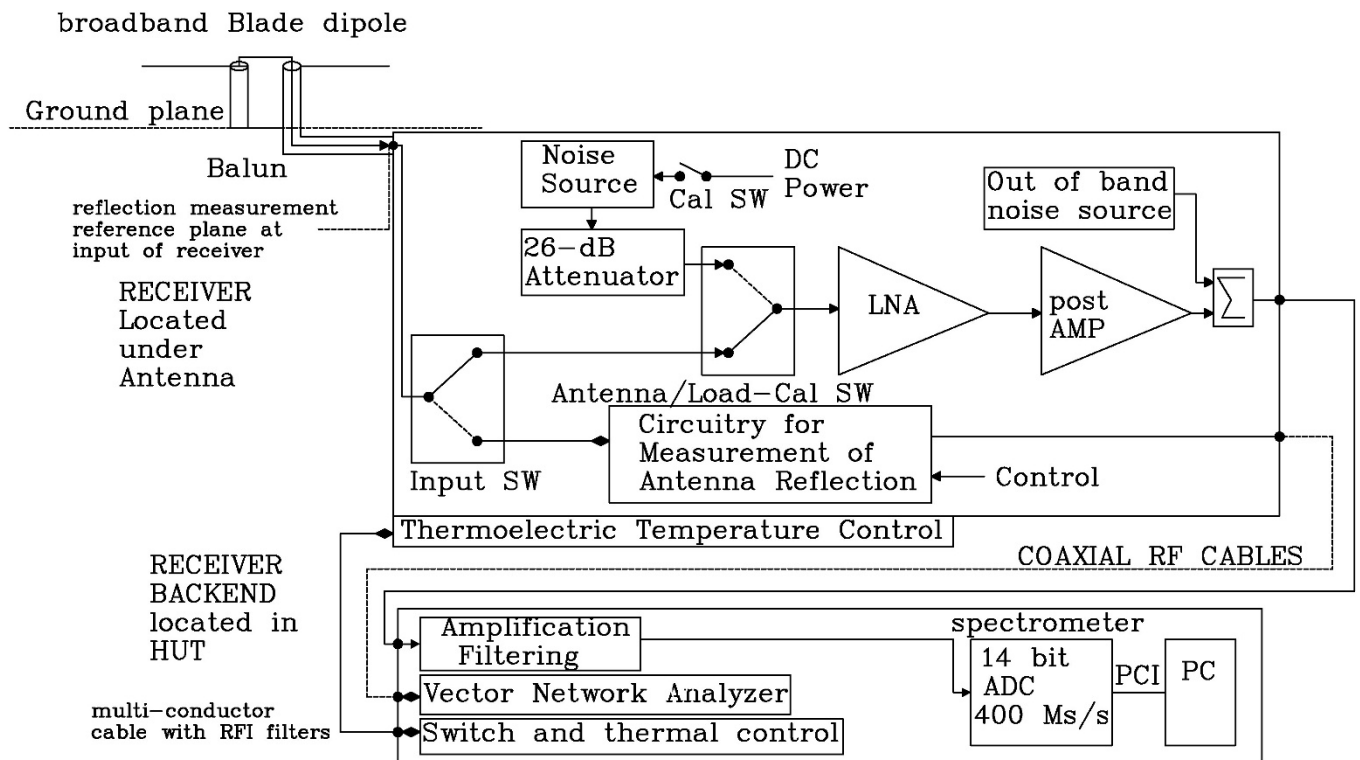
**Data availability.** The data that support the findings of this study are available from the corresponding author on reasonable request.

**Code availability.** The code that supports the findings of this study is available from the corresponding author on reasonable request.

32. Bowman, J. & Rogers, A. E. E. VHF-band RFI in geographically remote areas. In *Proc. RFI Mitigation Workshop* id.30, <https://pos.sissa.it/107/030/pdf> (Proceedings of Science, 2010).
33. Bowman, J. D. & Rogers, A. E. E. Lower Limit of  $\Delta z > 0.06$  for the duration of the reionization epoch. *Nature* **468**, 796–798 (2010).
34. Monsalve, R. A., Rogers, A. E. E., Bowman, J. D. & Mozdzen, T. J. Calibration of the EDGES high-band receiver to observe the global 21 cm signature from the epoch of reionization. *Astrophys. J.* **835**, 49 (2017).
35. Mozdzen, T. J., Bowman, J. D., Monsalve, R. A. & Rogers, A. E. E. Improved measurement of the spectral index of the diffuse radio background between 90 and 190 MHz. *Mon. Not. R. Astron. Soc.* **464**, 4995–5002 (2017).
36. Raghunathan, A., Shankar, N. U. & Subrahmanyam, R. An octave bandwidth frequency independent dipole antenna. *IEEE Trans. Antenn. Propag.* **61**, 3411–3419 (2013).
37. Ellingson, S. W. Antennas for the next generation of low-frequency radio telescopes. *IEEE Trans. Antenn. Propag.* **53**, 2480–2489 (2005).
38. Roberts, W. K. A new wide-band balun. *Proc. IRE* **45**, 1628–1631 (1957).

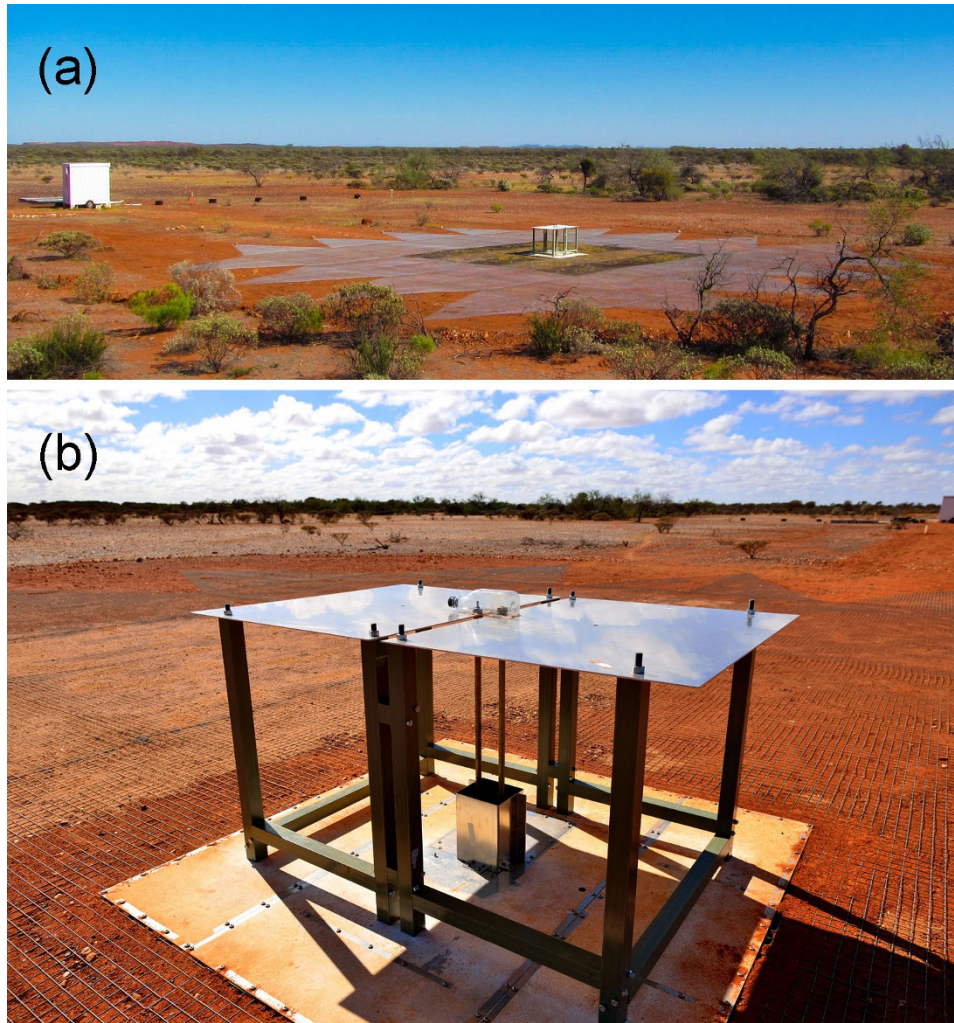
39. Bowman, J. D., Rogers, A. E. E. & Hewitt, J. N. Toward empirical constraints on the global redshifted 21 cm brightness temperature during the epoch of reionization. *Astrophys. J.* **676**, 1–9 (2008).
40. Rogers, A. E. E., Pratap, P., Carter, J. C. & Diaz, M. A. Radio frequency interference shielding and mitigation techniques for a sensitive search for the 327 MHz line of deuterium. *Radio Sci.* **40**, RS5S17 (2005).
41. Singh, S. *et al.* SARAS 2: a spectral radiometer for probing cosmic dawn and the epoch of reionization through detection of the global 21 cm signal. Preprint at <https://arxiv.org/abs/1710.01101> (2017).
42. Price, D. C. *et al.* Design and characterization of the Large-Aperture Experiment to Detect the Dark Age (LEDA) radiometer systems. Preprint at <https://arxiv.org/abs/1709.09313> (2017).
43. Rogers, A. E. E. & Bowman, J. D. Absolute calibration of a wideband antenna and spectrometer for accurate sky noise temperature measurement. *Radio Sci.* **47**, RS0K06 (2012).
44. Hu, R. & Weinreb, S. A novel wide-band noise-parameter measurement. *IEEE Trans. Microw. Theory Tech.* **52**, 1498–1507 (2004).
45. Belostotski, L. A calibration method for RF and microwave noise sources. *IEEE Trans. Microw. Theory Tech.* **59**, 178–187 (2011).
46. Ramo, S. & Whinnery, J. R. *Fields and Waves in Modern Radio* Ch. 6 (Wiley, 1953).
47. Monsalve, R. A., Rogers, A. E. E., Mozdzen, T. J. & Bowman, J. D. One-port direct/reverse method for characterizing VNA calibration standards. *IEEE Trans. Microw. Theory Tech.* **64**, 2631–2639 (2016).
48. Sutinjo, A. T. *et al.* Characterization of a low-frequency radio astronomy prototype array in Western Australia. *IEEE Trans. Antenn. Propag.* **63**, 5433–5442 (2015).
49. Haslam, C. G. T., Salter, C. J., Stoffel, H. & Wilson, W. E. A 408 MHz all-sky continuum survey. II. The atlas of contour maps. *Astron. Astrophys. Suppl. Ser.* **47**, 1–143 (1982).
50. Chandrasekhar, S. *Radiative Transfer* (Courier Dover, 1960).
51. de Oliveira-Costa, A. *et al.* A model of diffuse Galactic radio emission from 10 MHz to 100 GHz. *Mon. Not. R. Astron. Soc.* **388**, 247–260 (2008).
52. Bernardi, G., McQuinn, M. & Greenhill, L. J. Foreground model and antenna calibration errors in the measurement of the sky-averaged  $\lambda$ 21 cm signal at  $z \sim 20$ . *Astrophys. J.* **799**, 90 (2015).
53. Mozdzen, T. J., Bowman, J. D., Monsalve, R. A. & Rogers, A. E. E. Limits on foreground subtraction from chromatic beam effects in global redshifted 21 cm measurements. *Mon. Not. R. Astron. Soc.* **455**, 3890–3900 (2016).
54. McKinley, B. *et al.* Low-frequency observations of the Moon with the Murchison widefield array. *Astron. J.* **145**, 23 (2013).
55. Seager, S., Sasselov, D. D. & Scott, D. How exactly did the Universe become neutral? *Astrophys. J. Suppl. Ser.* **128**, 407–430 (2000).





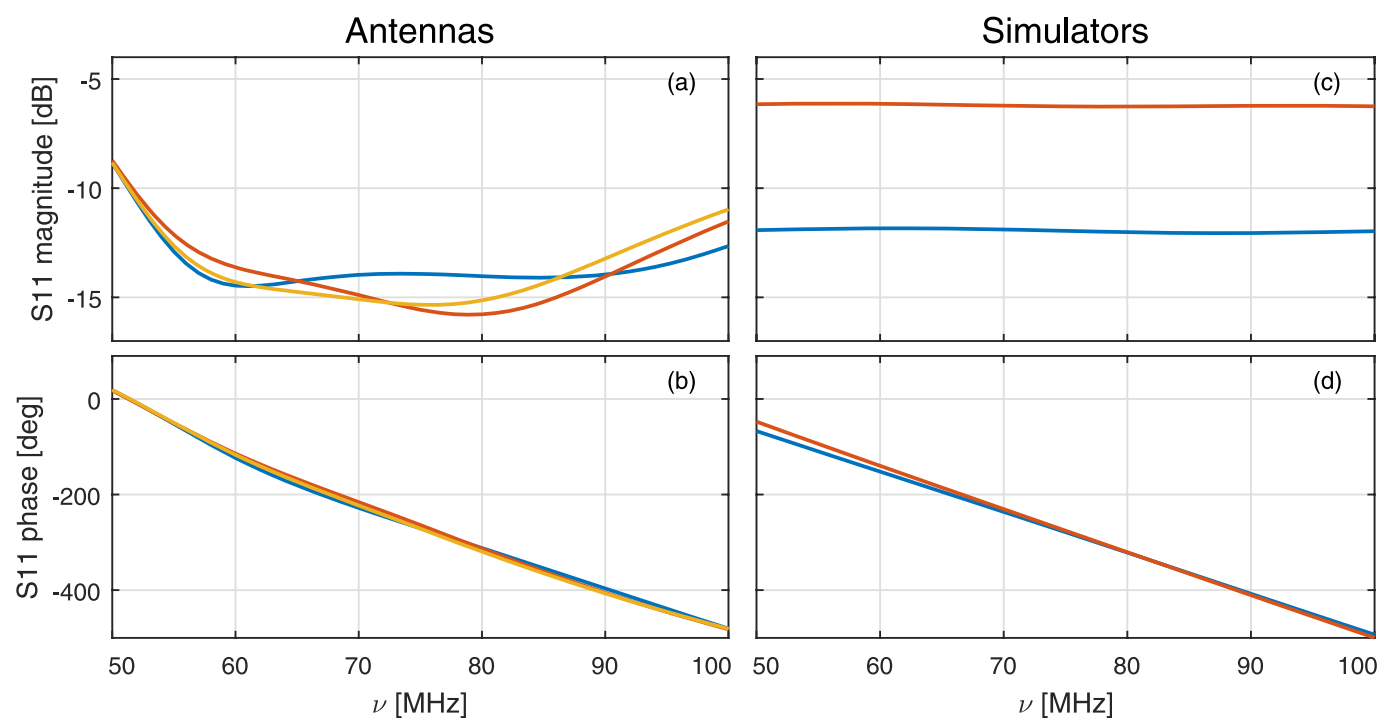
**Extended Data Figure 1 | Block diagram of the low-band system.** The inset images show: **a**, the capacitive tuning bar that feeds the dipoles at the top of the balun; **b**, the SubMiniature version A connector at the bottom of the balun coaxial transmission line where the receiver connects; **c**, the

low-1 receiver that is installed under its antenna with the ground-plane cover plate removed; and **d**, the inside of the low-1 receiver. The LNA is contained in the secondary metal enclosure in the lower-left corner of the receiver. SW, switch.



**Extended Data Figure 2 | Low-band antennas.** **a**, The low-1 antenna with the  $30\text{ m} \times 30\text{ m}$  mesh ground plane. The darker inner square is the original  $10\text{ m} \times 10\text{ m}$  mesh. The control hut is 50 m from the antenna. **b**, A close view of the low-2 antenna. The two elevated metal panels form

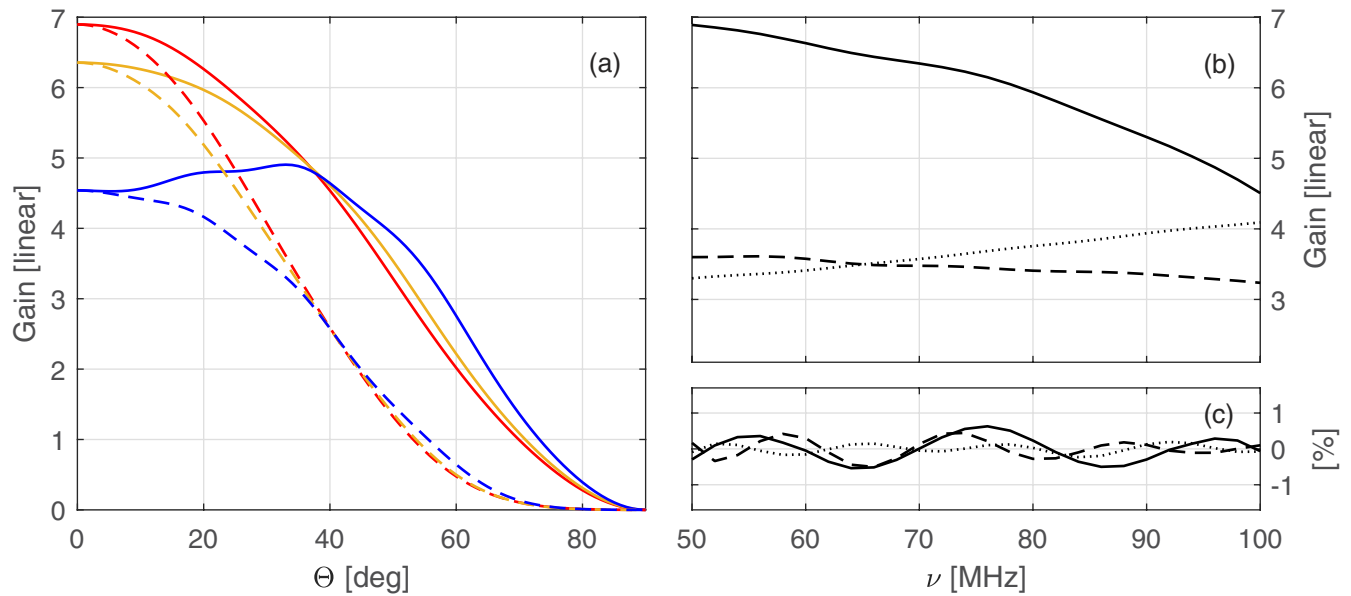
the dipole-based antenna and are supported by fibreglass legs. The balun consists of the two vertical brass tubes in the middle of the antenna. The balun shield is the shoebox-sized metal shroud around the bottom of the balun. The receiver is under the white metal platform and is not visible.



**Extended Data Figure 3 | Antenna and simulator reflection coefficients.** **a, b,** Measurements of the reflection coefficient magnitude (**a**) and phase (**b**) are plotted for hardware configurations H2 (blue), H4 (red) and H6 (yellow). The antennas are designed identically (except H6 has the balun shield removed), but are tuned manually during installation by adjusting

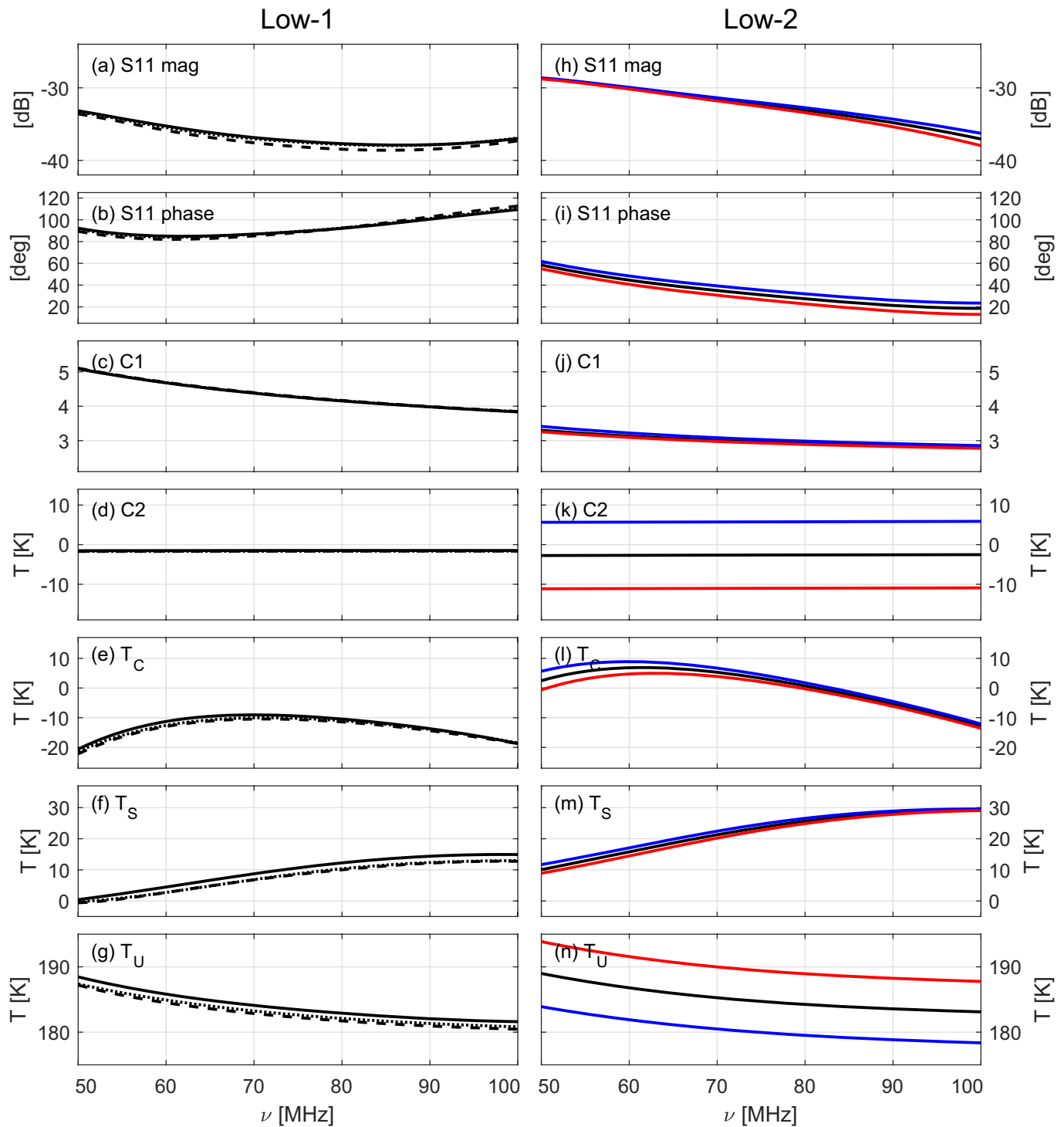
the panel separation and the height of the small metal plate that connects one panel to the centre conductor of the balun transmission line on the other. The measurements were acquired *in situ*. **c, d,** The red curve is the 10,000-K artificial antenna noise source and the blue curve is the 300-K mismatched load.





**Extended Data Figure 4 | Antenna beam model.** **a**, Beam cross-sections showing the gain in the plane containing the electric field (dashed) and in the plane containing the magnetic field (solid) from FEKO for the H2 antenna and ground plane over soil. Cross-sections are plotted at 50 MHz (red), 70 MHz (yellow) and 100 MHz (blue). **b**, Frequency dependence of the gain at zenith angle  $\Theta = 0^\circ$  (solid) and the 3-dB points at 70 MHz in the electric-field plane (dashed) and magnetic-field plane (dotted). **c**, Small

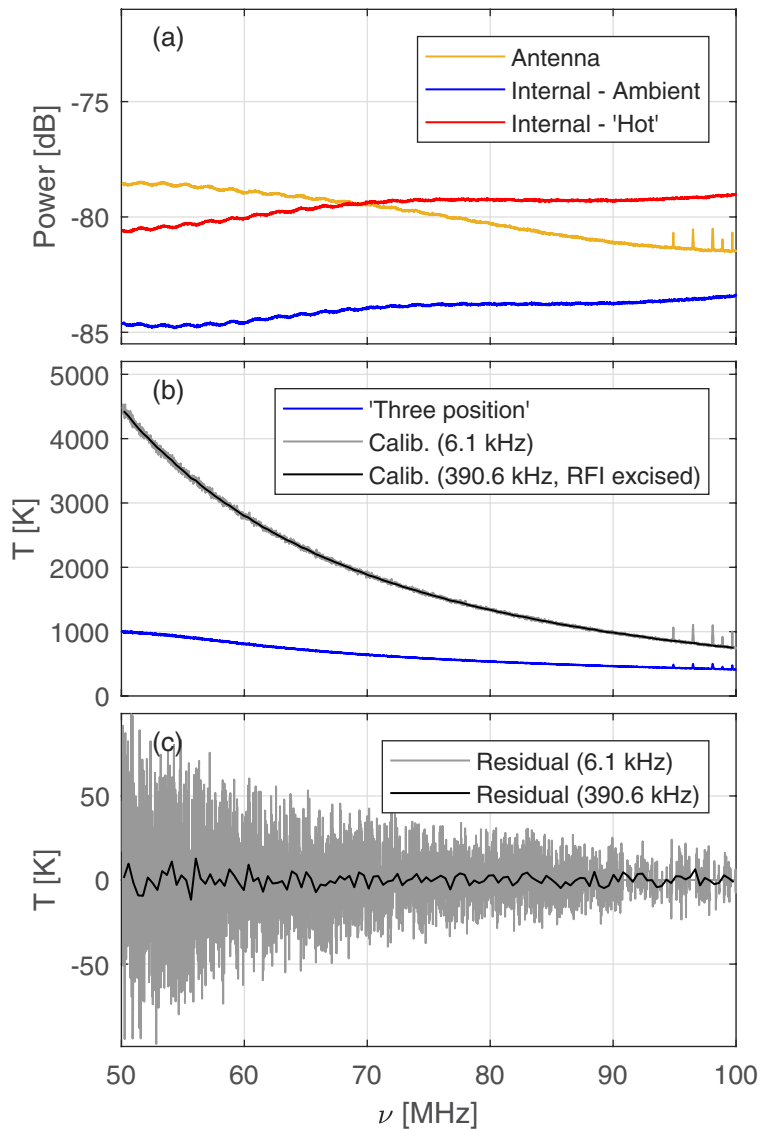
undulations with frequency, after a five-term polynomial (equation (2)) has been subtracted from each of the curves, are plotted as fractional changes in the gain. Simulated observations with this model yield residuals of 0.015 K (0.001%) to the five-term fit over the frequency range 52–97 MHz at GHA = 10 and residuals of 0.1 K (0.002%) at GHA = 0, showing that the cumulative beam yields less chromaticity than the approximately 0.5% variations in the individual points plotted.



#### Extended Data Figure 5 | Calibration parameter solutions.

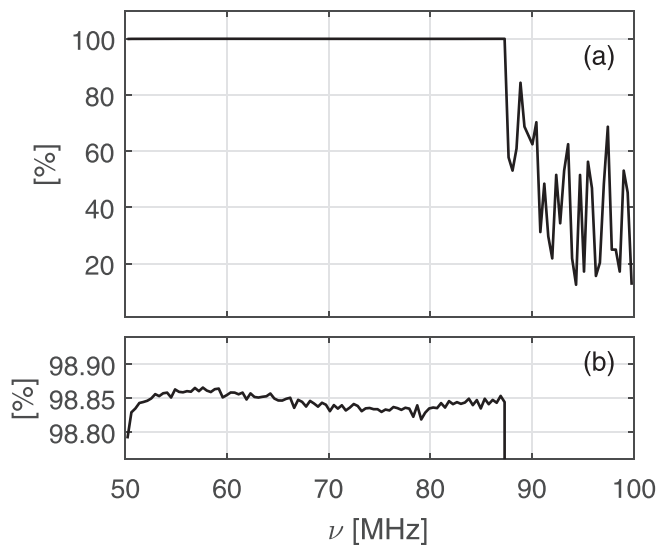
**a–g**, Solutions for the low-1 receiver at its fixed 25 °C operating temperature. It was calibrated on three occasions spanning two years, bracketing all of the low-1 observations reported. The first calibration was in August 2015 before commencing cases H1 and H2 (solid), the next was in May 2017 before H3 (dotted), and the final was in

September 2017 after the conclusion of H3 (dashed). **h–n**, Solutions for the low-2 receiver controlled to three different temperatures: 15 °C (blue), 25 °C (black) and 35 °C (red). The parameters C1 and C2 are scale and offset factors, respectively;  $T_C$ ,  $T_S$  and  $T_U$  are noise-wave parameters ( $T_S$  is not the spin temperature here; see ref. 34 for details); S11 is the LNA input reflection coefficient.

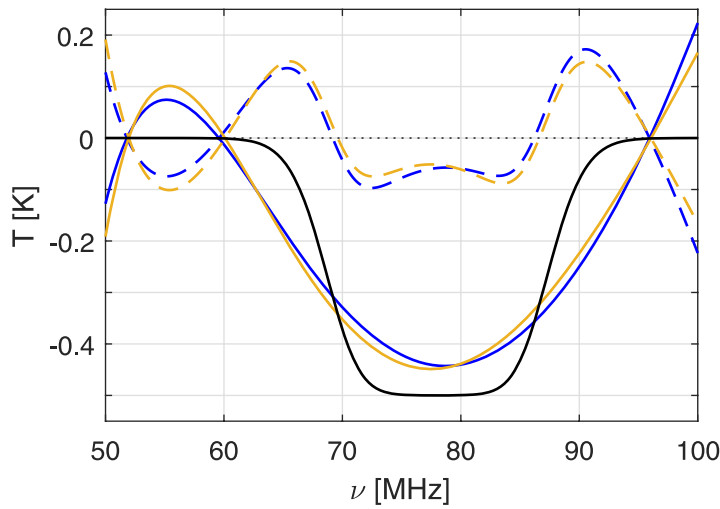


**Extended Data Figure 6 | Raw and processed spectra.** **a**, Typical raw 13-s spectra from H2 for each of the receiver's 'three position' switch states. The small spikes on the right of the antenna spectrum are FM radio stations. **b**, The spectrum has been partially calibrated ('Three position') using the three raw spectra to correct gain and offset contributions in the receiver and cables, then fully calibrated (Calib.) by applying the calibration parameter solutions from the laboratory to yield the sky temperature. **c**, Residuals to a fit of the fully calibrated spectrum with the five-term polynomial foreground model (equation (2)). In **b** and **c**, the frequencies listed in the legend give the binning used for each curve.

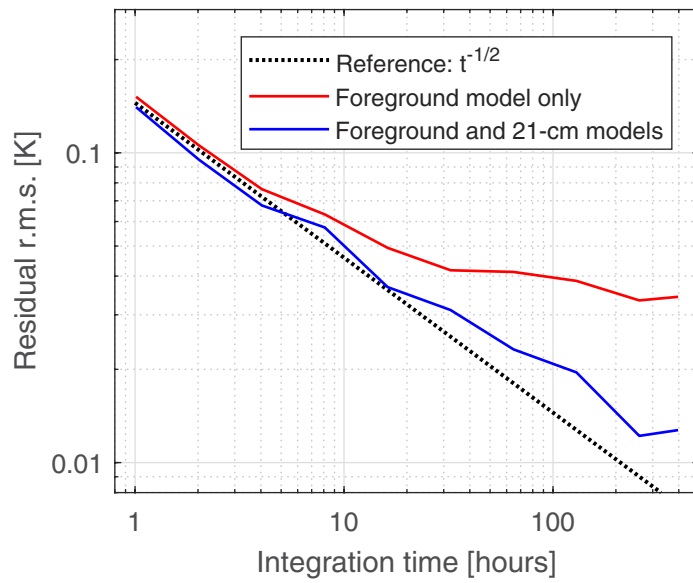




**Extended Data Figure 7 | Normalized channel weights.** The fraction of data integrated for each 390.6-kHz spectral bin are shown. **a**, The FM band causes the low weights above 87 MHz, because many 6.1-kHz raw spectral channels in this region are removed for all times. The weights are nearly identical across all hardware cases (H1–H6). **b**, A close-up showing the weights below the FM band, where there is little RFI to remove.

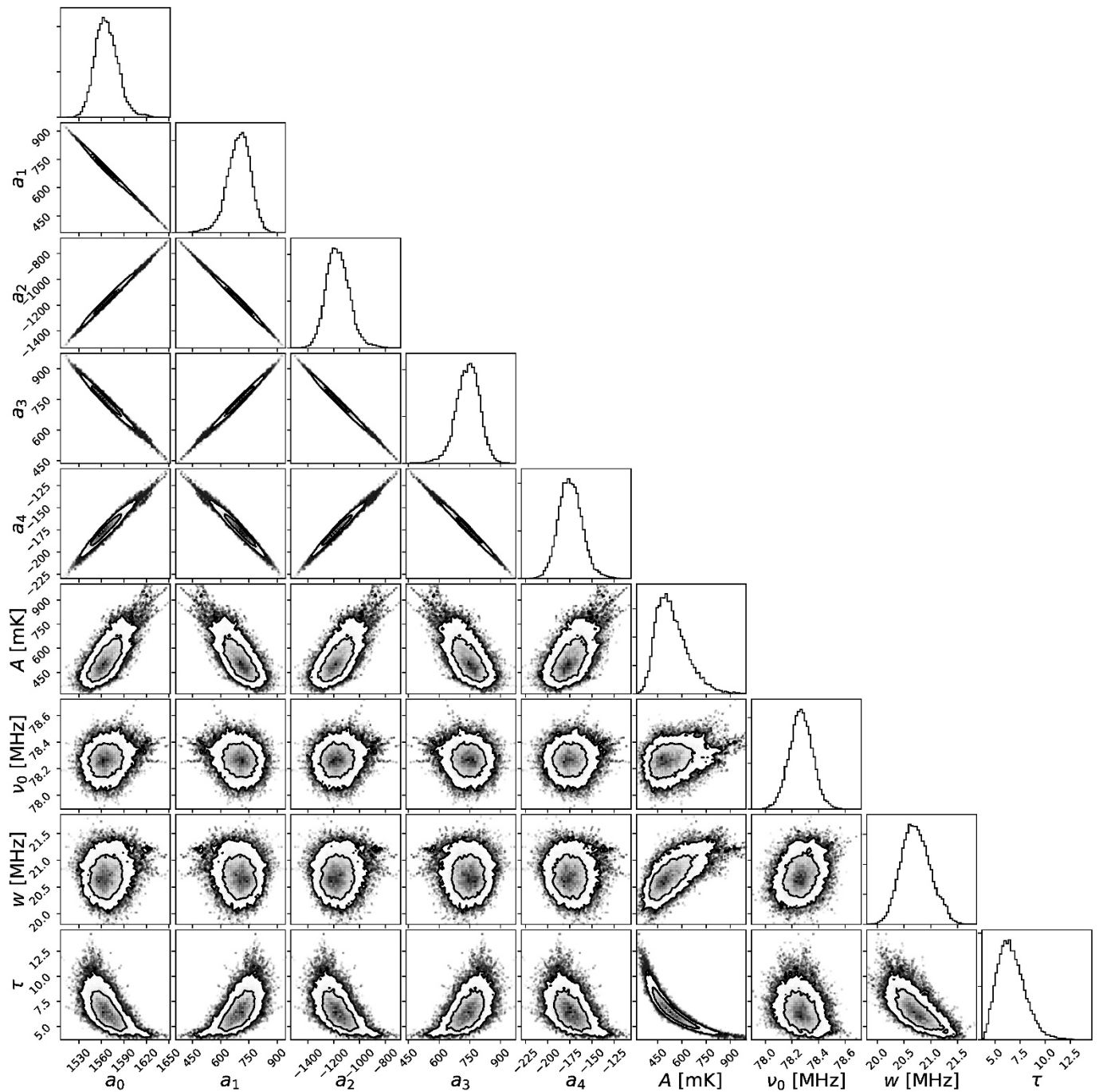


**Extended Data Figure 8 | Residuals to the 21-cm profile model.** The black curve shows the best-fitting 21-cm profile model derived from the observations. The solid blue and yellow curves show fits to the model profile using the physical (equation (1)) and five-term polynomial (equation (2)) foreground models, respectively. The dashed lines show the residuals after subtracting the fits from the model. These residuals are similar to those found when fitting the observations using only a foreground model (Fig. 1b).



**Extended Data Figure 9 | Residual r.m.s. as a function of integration time.**  
The curves show the residual r.m.s. after a best-fitting model is removed at each integration time for the H2 dataset.





**Extended Data Figure 10 | Parameter estimation.** Likelihood distributions for the foreground and 21-cm model parameters are shown for the H2 dataset. Contours are drawn at the 68% and 95% probability levels. The foreground polynomial coefficients ( $a_n$ ) are highly correlated

with each other, whereas the 21-cm model parameters are largely uncorrelated, except for the profile amplitude ( $A$ ) and flattening ( $\tau$ ). Systematic uncertainties from the verification hardware cases are not presented here.

**Extended Data Table 1 | Best-fitting parameter values for the 21-cm absorption profile for representative verification tests**

Configuration	Sky Time (hours)	SNR	Centre Frequency (MHz)	Width (MHz)	Amplitude (K)
<b>Hardware configurations (all P6)</b>					
H1 – low-1 10x10 ground plane	528	30	78.1	20.4	0.48
H2 – low-1 30x30 ground plane	428	52	78.1	18.8	0.54
H3 – low-1 30x30 ground plane and recalibrated receiver	64	13	77.4	19.3	0.43
H4 – low-2 NS	228	33	78.5	18.0	0.52
H5 – low-2 EW	68	19	77.4	17.0	0.57
H6 – low-2 EW and no balun shield	27	15	78.1	21.9	0.50
<b>Processing configurations (all H2 except P17)</b>					
P3 – No beam correction		19	78.5	20.8	0.37
No beam correction (65-95 MHz)		25	78.5	18.6	0.47
HFSS beam model		34	78.5	20.8	0.67
FEKO beam model		48	78.1	18.8	0.50
P4 – No loss corrections		25	77.4	18.6	0.44
P7 – 5-term foreground polynomial (60-99 MHz)		21	78.1	19.2	0.47
P8 – Physical foreground model (51-99 MHz)		37	78.1	18.7	0.53
P14 – Moon above horizon		44	78.1	18.8	0.52
Moon below horizon		40	78.5	18.7	0.47
P17 – 15°C calibration (61-99 MHz, 5-term)		25	78.5	22.8	0.64
35°C calibration (61-99 MHz, 5-term)		16	78.9	22.7	0.48

Model fits were performed by using a grid search with fixed  $\tau = 7$ . Sky time is the amount of time spent by the receiver in the antenna switch state and is 33% of wall-clock time. The data acquisition system has a duty cycle of about 50% and a spectral window function efficiency of about 50%, yielding effective integration times that are a factor of four smaller than the listed sky times. SNR, signal-to-noise ratio.

Extended Data Table 2 | Recovered 21-cm profile amplitudes for various GHAs

Galactic Hour Angle (GHA)	SNR	Amplitude (K)	Sky Temperature (K)
6-hour bins			
0	8	0.48	3999
6	11	0.57	2035
12	23	0.50	1521
18	15	0.60	2340
4-hour bins			
0	5	0.45	4108
4	9	0.46	2775
8	13	0.44	1480
12	21	0.57	1497
16	11	0.59	1803
20	9	0.66	3052

Each block is centred on the GHA listed. The 6-h bins used the five-term physical foreground model (equation (1)) fitted simultaneously with the 21-cm profile amplitude between 64 MHz and 94 MHz. The 4-h bins used a six-term polynomial foreground model (equation (2)) fitted between 65 MHz and 95 MHz. All data are from hardware configuration H2. Sky temperatures are reported at 78 MHz.